Deng, L., Han, S., Chen, H., Yang, L., **Guo, P.**, Shi, Z., **Zhang, H.** (2026):
Regulating interfacial electron flow in $Cu_2S@Co_3S_4$ Core–Shell heterostructures promoting H_2O_2 activation for singlet oxygen generation to efficiently degrade tetracycline
Sep. Purif. Technol. **394, Part 3** , art. 137618

Graphic Abstract.docx

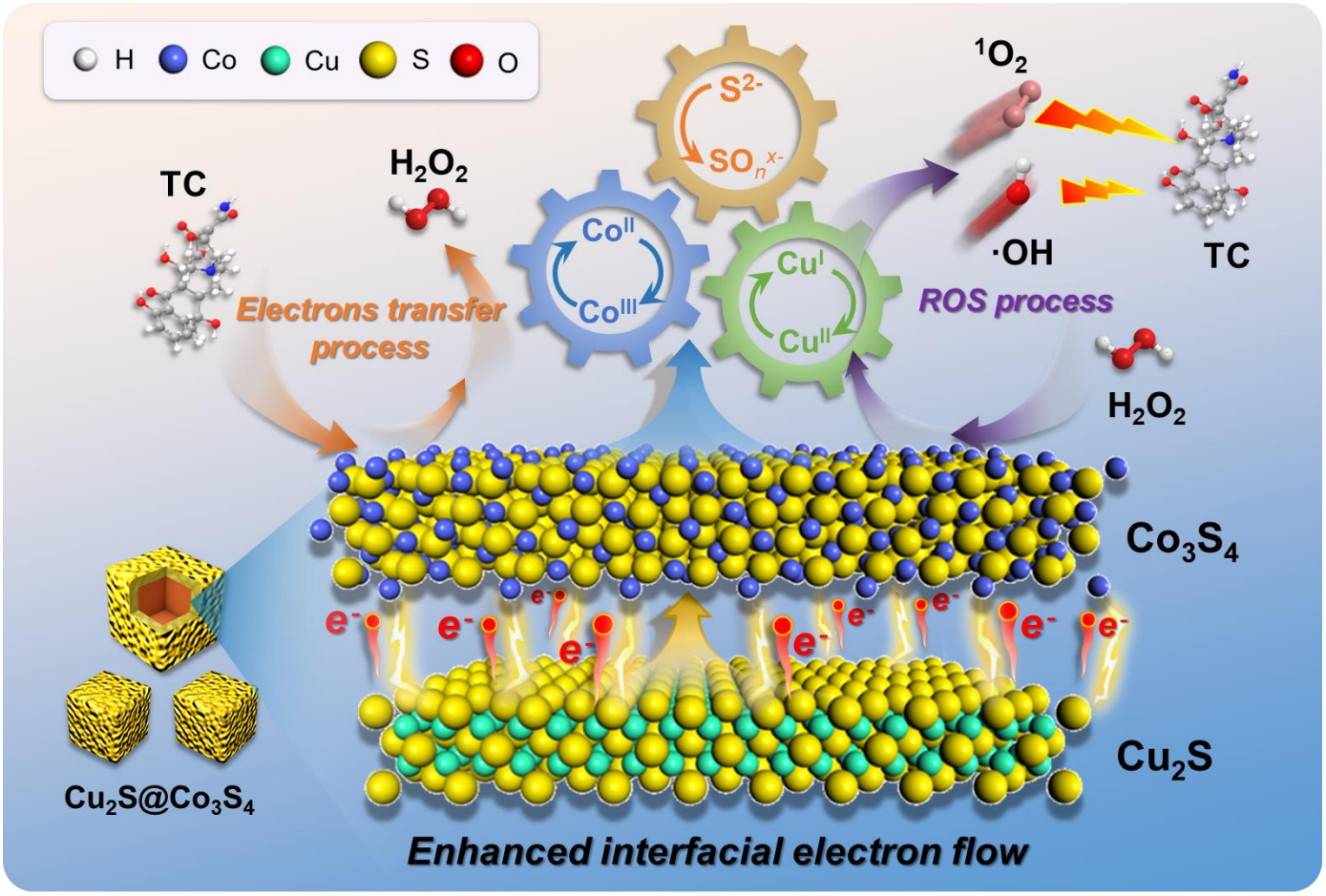

Regulating interfacial electron flow in $Cu_2S@Co_3S_4$ Core–Shell heterostructures promoting H_2O_2 activation for singlet oxygen generation to efficiently degrade tetracycline

Lin Deng[a], Shuo Han[a], Hangjie Chen[a], Lingfang Yang[a], Pengpeng Guo[b], Zhou Shi[a], Haojie Zhang[a,b,*]

a. Key Laboratory of Building Safety and Energy Efficiency, Ministry of Education, College of Civil Engineering, Hunan University, Changsha 410082, China

b. Department of Technical Biogeochemistry, Helmholtz Centre for Environmental Research – UFZ, Leipzig 04318, Germany

*Corresponding author
E-*mail address*: zhj95@hnu.edu.cn (H. Zhang)

Abstract

The widespread use and improper discharge of tetracycline (TC) pose significant threats to environmental safety and human health, necessitating the development of efficient removal technologies. Herein, a core-shell heterostructure, $Cu_2S@Co_3S_4$, was successfully synthesized via a hydrothermal method for activating H_2O_2 to degrade TC. Comprehensive characterization confirmed the well-defined cubic morphology and intimate interfacial contact between the Cu_2S core and Co_3S_4 shell. The optimized $Cu_2S@Co_3S_4$ demonstrated outstanding catalytic performance, remarkably removing over 97% of TC within 30 min and achieving a rate constant of 0.11 min^{-1}. This surpassed pure Co_3S_4 (0.004 min^{-1}) and Cu_2S (0.030 min^{-1}) by factors of 27.5 and 3.6, respectively. The system demonstrated high efficiency across a broad pH range (5–11) and showed strong resistance to common interfering ions. Mechanistic investigations, including quenching experiments, EPR analysis, and DFT calculations, revealed that $^1O_2$ was the predominant reactive species. The internal electron transfer from Cu_2S to Co_3S_4 enhanced H_2O_2 adsorption and activation, facilitating efficient electron transfer from TC to the surface-activated H_2O_2 complex. Besides, the redox cycles of Cu^+/Cu^{2+} and Co^{2+}/Co^{3+}, promoted by low-valence sulfur, sustained the catalytic activity. Degradation pathways were proposed, and toxicity assessment indicated the effective detoxification of TC. This work provides a highly efficient and stable heterostructured catalyst and offers deep insights into the H_2O_2 activation mechanism dominated by $^1O_2$ for antibiotic wastewater remediation.

Keywords: AOPs; Co_3S_4; Cu_2S; Tetracycline degradation; $^1O_2$; Electron transfer process

1. Introduction

Tetracycline (TC) is one of the most commonly used antibiotics for treating bacterial infections in human medicine and animal husbandry [1]. Globally, annual antibiotic consumption is estimated to be between 100,000 and 200,000 tons [2]. In livestock and aquaculture operations, only 20–30% of administered TC is absorbed and utilized by animals; the remainder is excreted as metabolites and released into surface water, groundwater, soil, and sediments [3]. Antibiotics, with their complex molecular structures, inhibit or disrupt bacterial growth [4]. The persistence of TC compounds in the environment promotes the development of antibiotic-resistant pathogens, posing serious threats to ecological balance and public health [5]. Hence, there is an urgent need to develop efficient and robust methods for TC removal to protect environmental safety and human health.

Advanced oxidation processes (AOPs), generating reactive oxygen species (ROS, e.g., •OH, $SO_4^{\bullet-}$, etc.), are widely used for the efficient removal of organic contaminants in drinking water production, elimination of recalcitrant micropollutants in wastewater treatment, and disinfection strategies [6]. A major advantage of AOPs over conventional treatment technologies is their ability to effectively degrade refractory compounds without producing secondary waste streams, a common issue in membrane-based processes [7]. In particular, Fenton and Fenton-like systems based on H_2O_2 activation have attracted growing interest due to their operational simplicity and high efficiency [8]. Common activation approaches include photocatalysis, electrocatalysis, and the use of transition metals (e.g., Fe [9], Cu [10]) and bimetallic catalyst activation [11]. The reaction rate constant between Cu(I) and H_2O_2 (10^4 M^{-1} s^{-1}) is significantly higher than

that of Fe(II) (76 M^{-1} s^{-1}), which makes copper-containing solid catalysts (such as zero-valent copper [12], copper oxides [13], and copper-based layered hydroxides [14]) promising alternatives to conventional iron-based catalysts [15].

Core–shell nanostructures, with tunable internal voids and flexible manipulation of core, shell, and void configurations, have attracted considerable interest in energy storage, sensing, and catalysis [16,17]. The interior voids facilitate efficient mass transport and provide substantial space for catalytic reactions. Moreover, adjustable structural features enable the exposure of diverse active sites, enhancing the adsorption and conversion of intermediates [18,19]. Heterostructured metal sulfides, constructed from interfaces between two distinct metal sulfides, demonstrate significantly improved catalytic activity compared to their single-component counterparts [20].

Owing to the superior catalytic properties of cobalt, considerable research has focused on heterogeneous cobalt catalysts, such as cobalt oxides, cobalt-containing mixed metal oxides, and supported cobalt materials [21,22]. Sulfur, with its low electronegativity and high ionization energy, serves as an effective coordinating element. Unsaturated sulfur atoms on transition metal sulfide surfaces can capture protons, exposing reduced metal active sites [23]. Low-valent sulfur species (S^{2-}, S_2^{2-}) in copper sulfides facilitate the reduction of Cu(II) to Cu(I), enhancing catalytic activity [24]. Sulfur coordination in structures such as MoS_2@Co_3S_4 promotes efficient electron-hole separation and increases active site accessibility, boosting sulfamethoxazole degradation [25].

Based on this rationale, we hypothesize that a Cu_2S@Co_3S_4 composite, synthesized by growing Co_3S_4 on Cu_2S, can function as a highly efficient catalyst for H_2O_2 activation

to degrade refractory organic pollutants. Herein, $Cu_2S@Co_3S_4$ was prepared via a hydrothermal route. Its morphology, crystal structure, and chemical composition were systematically characterized. The effects of catalyst dosage, H_2O_2 concentration, initial solution pH, and coexisting ions on TC degradation were evaluated. ROS generation and contribution were elucidated through EPR spectroscopy and quenching experiments. The adsorption energy of H_2O_2 at the catalyst interface and the number of electrons transferred were obtained through DFT calculations. A plausible mechanism for TC degradation in the $Cu_2S@Co_3S_4/H_2O_2$ system was proposed, along with identification of degradation intermediates and pathways.

2. Experimental methods

2.1. Chemicals

TC, furfuryl alcohol (FFA), tert-butyl alcohol (TBA), methanol (MeOH), 1,4-benzoquinone (BQ), methyl phenyl sulfoxide (PMSO), and methyl phenyl sulfone ($PMSO_2$) were obtained from Macklin Biochemical Technology Co., Ltd. (Shanghai, China). Hydrogen peroxide (H_2O_2, 30%), 5,5Dimethyl-1-pyrroline N-oxide (DMPO), 2,2,6,6-tetra-methyl-4-piperidone (TEMP) were purchased from Sigma-Aldrich Chemical Co., Ltd. (China). $CuCl_2·2H_2O$, $CoCl_2·6H_2O$, sodium citrate dihydrate ($Na_3C_6H_5O_7·2H_2O$), L-ascorbic acid ($C_6H_8O_6$), urea (CH_4N_2O), thioacetamide (C_2H_5NS), acetic acid (HAc), nitrobenzene (NB), NaOH, HCl, NaCl, $NaNO_3$, Na_2SO_4, and Na_2CO_3 were purchased from Sinopharm Chemical Reagent Co., Ltd. (Shanghai, China). All chemicals were analytical grade and used without further purification. Ultra-pure water (18.25 MΩ·cm) was prepared using a Millipore system (Bedford, USA).

2.2. Catalyst synthesis and characterizations

Synthesis of Cu_2O nanocubes. 2 mmol $CuCl_2 \cdot 2H_2O$ and 1 mmol trisodium citrate were dissolved in 160 mL deionized water. Then, 40 mL of 1.25 M NaOH aqueous solution was added dropwise under magnetic stirring for 5 min, changing the solution color from light blue to dark blue. Subsequently, 100 mL of 0.03 M L-ascorbic acid solution was introduced, and the reaction proceeded for 10 min. The mixture was aged at room temperature for 1 h. The precipitate was collected by vacuum filtration, washed with deionized water and anhydrous ethanol, and dried under vacuum at 60 °C for 12 h.

Synthesis of $Cu_2S@Co_3S_4$. A total of 71.5 mg of the as-synthesized Cu_2O was dispersed in 15 mL deionized water under stirring for 10 min. Separately, a specific amount of $CoCl_2 \cdot 6H_2O$, 250 mg urea, and 150 mg (4 mmol) thioacetamide were dissolved in 25 mL anhydrous ethanol. The Cu_2O suspension was slowly poured into the ethanol solution. The mixture was stirred and sonicated for 5 min, transferred into a Teflon-lined autoclave, and maintained at 180 °C for 22 h. The product was collected via vacuum filtration, washed with deionized water and ethanol, and dried under vacuum at 60 °C for 12 h. Finally, the material was calcined at 450 °C for 1 h under nitrogen to obtain $Cu_2S@Co_3S_4$. Composites with nominal Cu:Co molar ratios of 4:1, 2:1, and 1:1 were synthesized by adding 29.7 mg, 59.5 mg, and 119.0 mg of $CoCl_2 \cdot 6H_2O$, respectively. For comparison, Cu_2S and Co_3S_4 were prepared under identical conditions without adding Cu_2O or cobalt chloride.

The synthesis procedure of $Cu_2S@Co_3S_4$ is illustrated in Scheme 1. Comprehensive characterization details is described in Text S1 in the Supplementary Material.

2.3. Degradation tests of TC

All degradation experiments were conducted in 100 mL glass beakers. Typically, 4

mg of catalyst was dispersed homogeneously in 50 mL of a 20 μM TC solution via ultrasonication for 1 min. The degradation process was initiated by adding H_2O_2 to achieve a final concentration of 5 mM. At predetermined intervals, 0.5 mL aliquots were collected, filtered through a 0.22 μm membrane, and quenched with 0.2 mL of methanol. The TC concentration was quantified using high-performance liquid chromatography (HPLC, Agilent 1260, USA) equipped with a Symmetry C18 column (150mm×4.6mm×5μm, Agilent, USA) and a VWD detector (Agilent, USA). All experiments were performed in triplicate, and the results are reported as mean values with standard deviations. The steady state concentration of •OH and $^1O_2$ calculation method, and DFT calculation method can be found in Text S2 and S3.

3. Results and discussion

3.1. Characterizations

The morphology of Cu_2O and Cu_2S@Co_3S_4 composite was characterized using scanning electron microscopy (SEM) and transmission electron microscopy (TEM). As shown in Figure 1a, Cu_2O exhibit a well-defined nanocube morphology with an average size of approximately 500 nm. Figure 1b shows that Cu_2S@Co_3S_4 composite retains the cubic framework of the Cu_2O precursor, with a rougher surface and an average size of 1 μm. The TEM image (Figure 1c) confirms the distinct cubic architecture. Energy-dispersive X-ray spectroscopy (EDS) elemental mapping Figure 1d–f demonstrates homogeneous distribution of Cu, Co, and S, with Co predominantly located on the outer region, indicating a core–shell structure of the as-synthesized Cu_2S@Co_3S_4.

Figure 1g and h shows the XRD patterns of Cu_2O, Cu_2S, Co_3S_4, and Cu_2S@Co_3S_4 composites with different molar ratios. In Figure 1g, the diffraction peaks observed at

29.6°, 36.5°, 42.4°, 52.6°, 61.5°, 73.7°, and 77.6° are indexed to the (110), (111), (200), (211), (220), and (222) crystal planes of Cu_2O (PDF#75-1531), respectively, confirming the successful synthesis of phase-pure Cu_2O. As show in Figure 1h, diffraction peaks at 27.7°, 32.1°, 46.0°, 54.5°, 67.1°, and 85.2° are indexed to the (111), (200), (220), (311), (400), and (422) crystal planes of Cu_2S (PDF#72-1966), respectively. Meanwhile, peaks at 16.3°, 26.8°, 31.5°, 41.8°, 50.3°, and 55.1° correspond to the (111), (220), (311), (331), (511), and (440) planes of Co_3S_4 (PDF#75-1561), respectively. No impurity peaks were detected, indicating successful preparation of a highly crystalline composite.

Electron paramagnetic resonance (EPR) spectroscopy is a highly sensitive technique used to characterize material defects by detecting unpaired electrons associated with such imperfections [26]. As shown in Figure S1, the EPR spectra of Cu_2S, Co_3S_4, and $Cu_2S@Co_3S_4$ all exhibit signals corresponding to sulfur vacancy (Sv). Among these, Co_3S_4 shows the most intense Sv signal, whereas both Cu_2S and the $Cu_2S@Co_3S_4$ composite display weaker and comparable signal intensities, suggesting similar sulfur vacancies contents in these two materials. The XRD signal intensities for Cu_2S and $Cu_2S@Co_3S_4$ are strikingly higher than those of CoS_2, demonstrating significantly greater crystallinity (Figure 1h). This clearly demonstrates that metal and sulfur atoms within Cu_2S and $Cu_2S@Co_3S_4$ are more fully integrated, leading to a substantially reduced defect density. This superior structural integrity further attests to their enhanced stability, which underpins sustained long-term catalytic performance.

X-ray photoelectron spectroscopy (XPS) was employed to analyze the elemental states and surface composition of the $Cu_2S@Co_3S_4$ composite. The XPS survey spectrum of $Cu_2S@Co_3S_4$ (Figure 2a) shows the main elements of $Cu_2S@Co_3S_4$ including Cu, Co

and S. Two characteristic peaks of Cu^{+} at 932.5 eV ($2p_{3/2}$) and 952.3 eV ($2p_{1/2}$) are found in the high-resolution Cu 2p spectrum (Figure 2b), consistent with the typical valence state in Cu_2S [27]. Additionally, peaks identified at 934.4 eV (Cu^{2+} $2p_{3/2}$) and 954.7 eV (Cu^{2+} $2p_{1/2}$), along with satellite features at 943.9 eV and 963.2 eV, are likely due to surface oxidation of Cu_2S [28]. The Co 2p spectrum (Figure 2c) reveals two spin-orbit doublets and two satellite peaks. The peaks at binding energies of 778.9 eV and 793.7 eV are assigned to Co^{3+} $2p_{3/2}$ and Co^{3+} $2p_{1/2}$, respectively, while those at 781.0 eV and 796.4 eV correspond to Co^{2+} $2p_{3/2}$ and Co^{2+} $2p_{1/2}$. Satellite peaks are observed at 784.4 eV and 801.1 eV. These spectral features align well with previously reported valence states of Co_3S_4 [29,30]. The S 2p spectrum (Figure 2d) can be deconvoluted into two spin-orbit doublets and an additional peak. The doublets consistent of components at 161.5 eV (S^{2-} $2p_{3/2}$), 162.7 eV (S^{2-} $2p_{1/2}$), 162.9 eV (S_2^{2-} $2p_{3/2}$), and 164.3 eV (S_2^{2-} $2p_{1/2}$), along with a peak at 168.4 eV attributed to SO_3^{2-} species [31].

3.2. Catalytic activity tests

The catalytic performance of the $Cu_2S@Co_3S_4$ composite for activating H_2O_2 toward TC degradation was systematically evaluated. As depicted in Figure 3a, control experiments revealed that neither H_2O_2 alone nor the Co_3S_4/H_2O_2 system achieved significant TC removal within 30 min, underscoring the limited non-catalytic oxidation and the low intrinsic activity of Co_3S_4. When employed as an adsorbent without H_2O_2, the $Cu_2S@Co_3S_4$ composite itself removed 51% of TC, while the Cu_2S/H_2O_2 system led to a 63% degradation. In stark contrast, all $Cu_2S@Co_3S_4$ composites with varying Cu:Co ratios, in the presence of H_2O_2 (5 mM) and catalyst (0.08 g/L), achieved exceptional TC removal exceeding 92%. Among them, the composite with a Cu:Co ratio

of 2:1 demonstrated the highest efficiency. The kinetic analysis (Figure 3b) further confirmed this trend, yielding pseudo-first-order kinetic rate constants (k) of 0.077 min^{-1}, 0.110 min^{-1}, and 0.076 min^{-1} for the composites with Cu:Co ratios of 4:1, 2:1, and 1:1, respectively. Impressively, the rate constant for the optimal $Cu_2S@Co_3S_4$ (2:1) was 27.5 times and 3.6 times greater than that of Co_3S_4 (0.004 min^{-1}) and Cu_2S (0.030 min^{-1}), respectively.

3.3. Influencing factors on TC degradation

The effects of various operational parameters, including catalyst dosage (0.04–0.16 g/L), H_2O_2 concentration (1–7 mM), initial pH (3–11), and coexisting ions (such as Cl^-, NO_3^-, SO_4^{2-}, and CO_3^{2-}) on TC degradation by the $Cu_2S@Co_3S_4/H_2O_2$ system are discussed below. As shown in Figure 3c, the degradation efficiency improved with increasing catalyst dosage. Specifically, when the dosage increased from 0.04 to 0.08 g/L, the TC removal rate rose from 85% to 97% within 30 min. This enhancement can be attributed to the increased number of active sites available for H_2O_2 activation and the consequent generation of reactive species [32]. However, further increases in catalyst dosage did not yield a significant enhancement in degradation efficiency, suggesting that excessive catalyst addition is unnecessary. Accordingly, a dosage of 0.08 g/L was selected as optimal for subsequent experiments. The concentration of H_2O_2 also played a critical role in the degradation process (Figure 3d). TC degradation improved slightly as the H_2O_2 concentration increased from 1 to 7 mM, which can be explained by the greater abundance of reactive species generated at higher H_2O_2 levels, promoting more efficient TC elimination [33]. Based on these results, an H_2O_2 concentration of 5 mM was chosen for further studies.

The initial solution pH also significantly influenced the degradation efficiency. As depicted in Figure 3e, high acidic conditions (pH=3) inhibited TC degradation. In contrast, over a broad pH range (5–11), the $Cu_2S@Co_3S_4/H_2O_2$ system maintained a TC removal efficiency exceeding 97%, indicating that the catalyst can perform effectively without pH adjustment, a notable advantage for practical applications. The inhibitory effect under acidic conditions may be due to H^+ ions scavenging •OH radicals ($H^+ + •OH + e^- \rightarrow H_2O$) [34]. thereby reducing oxidative capacity. Moreover, higher pH values promote the deprotonation of TC into anionic forms, which exhibit higher electron density and are more susceptible to attack by H_2O_2 and free radicals, facilitating molecular decomposition [35].

The effects common inorganic anions on TC degradation were investigated to simulate natural water conditions (Figure 3f). The presence of 5 mM Cl^- resulted in approximately 5% inhibition, likely due to the formation of less reactive chlorine species (e.g., $ClOH•^-$ via $•OH + Cl^- \rightarrow ClOH•^-$) [36]. Both NO_3^- and SO_4^{2-} showed slight inhibitory effects, possibly due to competitive adsorption at catalyst active sites [37]. In contrast, CO_3^{2-} enhanced degradation, potentially because it raises the solution pH and generates carbonate radicals that participate in electron transfer processes with aromatic rings in TC. It has been reported that TC degradation proceeds mainly through electron addition to aromatic rings rather than hydroxylation [38], a pathway further promoted by carbonate radicals. Despite the presence of these coexisting ions, the system still achieved over 90% TC removal, demonstrating robust performance and stability under environmentally relevant conditions.

The stability and practical applicability of solid catalysts hinge critically on their

recyclability. The recyclability of $Cu_2S@Co_3S_4$ was rigorously evaluated over five consecutive degradation cycles. Following each cycle, the catalyst was meticulously recovered, washed with ultrapure water and ethanol, and vacuum-dried prior to reuse. As shown Figure S2, the catalyst maintained a robust TC degradation efficiency of 80% even after five cycles, underscoring its satisfactory recyclability and structural stability. Analysis by atomic absorption spectrophotometry furthermore revealed that the leaching concentration of copper ions was 1.2 mg/L, which was below the stringent EU Drinking Water Directive limit of 2 mg/L. While no cobalt ion leaching was detected, unequivocally confirming the catalyst's high stability under operational conditions.

3.4. Identification of reactive species

The reactive species governing the TC degradation in the $Cu_2S@Co_3S_4/H_2O_2$ system were systematically identified through a combination of scavenging and spectroscopic techniques. TBA was applied as an effective quencher for •OH (rate constant: 3.8–7.6 × 10^8 M^{-1} s^{-1}) [39], FFA for both •OH (1.5 × 10^{10} M^{-1} s^{-1}) and $^1O_2$ (1.2 × 10^8 M^{-1} s^{-1}) [40], and BQ for $•O_2^-$ [41]. As shown in Figure 4a, the drastic inhibition by FFA pointed to $^1O_2$ as a pivotal species, the partial suppression by TBA indicated a secondary role for •OH, and the non-inhibition by BQ effectively excluded $•O_2^-$ as a primary contributor. This interpretation was directly validated by EPR spectroscopy, using DMPO and TEMP as spin-trapping agents to identify the ROS generated in the $Cu_2S@Co_3S_4/H_2O_2$ system. As shown in Figure 4b-d, no radical signals emerged in the absence of H_2O_2, demonstrating conclusively that $Cu_2S@Co_3S_4$ alone fails to generate radicals. However, distinct signals for DMPO-•OH, TEMP-$^1O_2$, and DMPO-$•O_2^-$ adducts emerged when both $Cu_2S@Co_3S_4$ and H_2O_2 were present, unequivocally verifying the generation of •OH, $^1O_2$, and $•O_2^-$

271 radicals.

272 To quantitatively differentiate the roles of ROS, the steady-state concentrations of
273 •OH and $^1O_2$ were measured, while $•O_2^-$ was excluded due to its low oxidative potential
274 (–0.2 V) [42]. As illustrated in Figure 5a, probe experiments using nitrobenzene (NB) and
275 FFA revealed that the steady-state concentration of $^1O_2$ was 3.39×10^{-10} M, which was
276 nearly two orders of magnitude higher than that of •OH (5.34×10^{-12} M). Additionally,
277 the potential formation of high-valent metal species was examined, but no conversion of
278 PMSO to $PMSO_2$ was observed (Figure 5b), confirming their absence. Together, the
279 quantitative predominance of $^1O_2$ and the exclusion of other potent oxidants definitively
280 establish $^1O_2$ as the primary species driving TC degradation.

281 The generation of $^1O_2$ in AOPs can originate from multiple pathways, such as light
282 irradiation [43], energy transfer from dissolved oxygen [44], or the recombination of $•O_2^-$
283 radicals [45]. To distinguish the operative mechanism in the $Cu_2S@Co_3S_4/H_2O_2$ system,
284 were conducted degradation experiments under critical controlled conditions. The results
285 (Figure 5c) show that excluding either light (dark conditions) or DO (N_2 purging) did not
286 impair the reaction efficiency, thereby eliminating these two as major $^1O_2$ sources. This
287 experimental exclusion, coupled with the earlier finding that $•O_2^-$ quenching did not
288 inhibit degradation, allow us to definitively rule out the recombination route. Therefore,
289 the evidence collectively points to the direct activation of H_2O_2 at the catalyst interface
290 as the principal mechanism for $^1O_2$ production.

291 3.5. Enhanced electron transfer process

292 We investigated the electron transfer process, a pivotal degradation mechanism in
293 heterogeneous catalysis [46], by analyzing open circuit potential (OCP). The potential

increase upon the addition of H_2O_2 (Figure 5d) corresponded to the adsorption and surface complexaion of H_2O_2 (forming H_2O_2*). The swift potential equilibration observed in the Cu_2S@Co_3S_4/H_2O_2 system pointed to a highly efficient interfacial charge transfer with the Cu_2S@Co_3S_4 heterojunction. This was directly explained by our DFT results (Figure S3), which visualized electron redistribution and a net transfer of 0.12 electrons from Cu_2S to Co_3S_4. This electron enrichment on Co_3S_4 optimally primed the surface for H_2O_2 activation. The subsequent potential surge upon TC addition provided direct electrochemical evidence that TC acted as an electron donor to the activated H_2O_2* complex [47]. The magnitude of the total potential change (0.07 V) was greatest for the Cu_2S@Co_3S_4 composite, offering definitive proof that the heterojunction structure fostered the most powerful electron transfer process, thereby driving the exceptional catalytic activity.

Furthermore, DFT calculations were performed to compare the H_2O_2 adsorption behavior and electron transfer capability of Co_3S_4 and Cu_2S@Co_3S_4 (Figure 5e and f). The calculated adsorption energy for H_2O_2 on Cu_2S@Co_3S_4 was –1.91 eV, substantially more negative than that on pure Co_3S_4 (–0.37 eV), indicating a much stronger affinity and more favorable capture of H_2O_2 by the composite, which promoted its subsequent activation. The enhanced activation was further evidenced by the pronounced elongation of the O–O bond in H_2O_2 adsorbed on Cu_2S@Co_3S_4, which was stretched to 2.69 Å, suggesting a greatly facilitated cleavage tendency. Differential charge density analysis (where red and blue regions denote electron depletion and accumulation, respectively) provided deeper insight into the interfacial electron transfer. The internal electron donation from the Cu_2S core to the Co_3S_4 shell (0.12 e^-) created an electron-rich surface,

enabling Co_3S_4 to transfer a significantly large number of electrons to the adsorbed H_2O_2. Consequently, H_2O_2 gained 0.41 e^- from the $Cu_2S@Co_3S_4$ composite, a value six times greater than the 0.07 e^- transferred from Co_3S_4 alone. These results collectively offer compelling theoretical evidence that the synergistic electron transfer within the $Cu_2S@Co_3S_4$ heterostructure is crucial for the highly efficient activation of H_2O_2.

3.6. Possible H_2O_2 activation mechanism by $Cu_2S@Co_3S_4$

To elucidate the TC degradation mechanism in the $Cu_2S@Co_3S_4/H_2O_2$ system, the catalyst was characterized by XPS before and after the reaction (Figure 6a). As shown in Figure 6b, the Cu 2p spectra demonstrate a marked shift in valence states: the proportion of Cu^+ decreased from 79.0% to 62.9%, while Cu^{2+} increased from 21.0% to 37.1%, directly evidencing in oxidation of Cu^+ and its crucial role in the catalytic cycle. Parallel changes were observed in the Co 2p spectrum (Figure 6c), where the Co^{3+}/Co^{2+} ratio increased, confirming the involvement of cobalt redox pairs. Additionally, the S 2p spectra (Figure 5d) indicated consumption of low-valence S^{2-} species and a notable rise in sulfate content (from 17% to 35%), underscoring the participation of sulfur in redox cycles. This is consistent with literature suggesting that sulfur moieties facilitate the reduction of high-valance metals (e.g., Cu^{2+} to Cu^+), thereby sustaining catalytic activity [48].

Integrating these spectroscopic insights, we propose a concerted activation mechanism (Figure 6e). The process begins with H_2O_2 adsorption and activation on Co sites of $Cu_2S@Co_3S_4$, initiating a redox cycle (Eqs. 4 and 5) [49]. Simultaneously, H_2O_2 penetrating to the core interacts with Cu_2S, triggering a complementary Cu^+/Cu^{2+} redox cycle (Eqs. 1 and 2) [50]. Critically, the low-valence sulfur acts as an electron reservoir,

efficiently regenerating Cu^{+} from Cu^{2+} and Co^{2+} from Co^{3+} (Eqs. 3 and 6) [49,51], which amplifies the production of •OH via Eqs. 1 and 4. Beyond •OH generation, the system engages multiple radical pathways. Single-electron transfer from H_2O_2 to Cu^{2+} yields HOO•/$•O_2^-$ (Eq. 2). while a parallel reaction at Co^{3+} sites produces $•O_2H$ radicals (Eq. 5). These species further react to form $•O_2^-$ (Eqs. 7–9) [49,52,53]. $^1O_2$ is then generated via three dominant routes: (i) oxidation of Cu^{2+} by HOO•/$•O_2^-$ (Eq. 10); (ii) interconversion and recombination of HOO•, $•O_2^-$, and •OH (Eqs. 11–15); and (iii) reactions between H_2O_2 and peroxide radicals (Eqs. 16 and 17). Finally, direct electron transfer from TC to the catalyst surface, enhanced by the internal electron flow between Cu_2S and Co_3S_4, constitutes a vital non-radical degradation pathway.

$$Cu^{+} + H_2O_2 \rightarrow Cu^{2+} + OH^{-} + •OH \quad (1)$$

$$Cu^{2+} + H_2O_2 \rightarrow Cu^{+} + H^{+} + HOO•/•O_2^{-} \quad (2)$$

$$Cu^{2+} + S^{2-} + H_2O \rightarrow Cu^{+} + SO_4^{2-} + 8H^{+} \quad (3)$$

$$Co^{2+} + H_2O_2 \rightarrow Co^{3+} + OH^{-} + •OH \quad (4)$$

$$Co^{3+} + H_2O_2 \rightarrow Co^{2+} + H^{+} + •O_2H \quad (5)$$

$$Co^{3+} + S^{2-}/S_2^{2-} \rightarrow Co^{2+} + Sn^{2-}/SO_x \quad (6)$$

$$HOO• \rightarrow •O_2^{-} + H^{+} \quad (7)$$

$$•OH^{-} + 2H_2O_2 \rightarrow •O_2^{-} + H_2O + 2H^{+} + •O_2H^{-} \quad (8)$$

$$•O_2H^{-} \rightarrow H^{+} + •O_2^{-} \quad (9)$$

$$Cu^{2+} + HOO•/•O_2^{-} \rightarrow Cu^{+} + H^{+} + {}^1O_2 \quad (10)$$

$$•O_2^{-} + H_2O \rightarrow {}^1O_2 + H_2O_2 + OH^{-} \quad (11)$$

$$•O_2^{-} + H^{+} \rightarrow HOO• \rightarrow H_2O_2 + {}^1O_2 \quad (12)$$

$$HOO• + •OH \rightarrow {}^1O_2 + OH^{-} \quad (13)$$

$$\bullet O_2^- + \bullet OH \rightarrow {}^1O_2 + OH^- \quad (14)$$

$$\bullet O_2^- + HOO\bullet \rightarrow {}^1O_2 + \bullet O_2H^- \quad (15)$$

$$HOO\bullet + H_2O_2 \rightarrow {}^1O_2 + \bullet OH + H_2O \quad (16)$$

$$\bullet O_2^- + H_2O_2 \rightarrow {}^1O_2 + \bullet OH + OH^- \quad (17)$$

3.7. Degradation pathways and toxicity analysis of intermediates

The degradation intermediates of TC by the $Cu_2S@Co_3S_4/H_2O_2$ system were identified by high-performance liquid chromatography-mass spectrometry (HPLC-MS). A total of 17 intermediates were detected (Figure S4 and Table S1), and three potential degradation pathways are proposed in Figure 7, involving terminal oxidation, dealkylation, deamidation, and ring-opening reactions [54]. In Pathway 1, a nucleophilic reaction yields intermediate P1 (m/z = 461), which is subsequently dehydrogenated via $\bullet O_2^-$ attack to form P2 (m/z = 459) [51], followed by deamidation to produce P3 (m/z = 416) [55]. Pathway 2 begins with the removal of two methyl groups from the tertiary amine, forming P4 (m/z = 417). This pathway then bifurcates: one branch proceeds through ring cleavage, dehydration, and loss of an amide group to generate P5 (m/z = 379) and P7 (m/z = 362). Cleavage of a two-carbon unit and carbonyl loss from P5 leads to P6 (m/z = 239) [56], while ring-opening of the carbonyl-containing moiety in P7 produces P8 (m/z = 318) [57], which further undergoes hydrolysis and decarbonylation to yield P6 as well. In Pathway 3, TC undergoes terminal oxidation to form P9 (m/z = 475), which is subsequently degraded via dealkylation and benzene ring cleavage to P10 (m/z = 362) [51], Subsequent removal of an amino group and a carbonyl leads to P11 (m/z = 309), followed by dehydration to form P12 (m/z = 242) [58]. Additionally, several small molecular intermediates were identified, including P13 (m/z = 239), P14 (m/z = 164) [55],

P15 (m/z = 132), P16 (m/z = 118), and P17 (m/z = 60) [51]. All these intermediates can be further mineralized into low-molecular-weight compounds such as H_2O, CO_2, and NO_3^- through ongoing reactions with $^1O_2$, •OH, and $•O_2^-$.

The developmental toxicity and mutagenicity of TC and its major degradation intermediates were predicted using the Toxicity Estimation Software Tool (T.E.S.T. Version 5.1.2) based on quantitative structure–activity relationship (QSAR) modeling. A shown in Figure S5, TC exhibits pronounced developmental toxicity (score: 0.86) and positive mutagenicity (score: 0.6). In contrast, most intermediates demonstrate reduced toxicity. Specifically, developmental toxicity decreases for all identified intermediates except P4, P8, and P12 (Figure S5a), and similarly, mutagenicity is lower for the majority of products (Figure S5b). These findings confirm that the $Cu_2S@Co_3S_4/H_2O_2$ system not only degrades TC effectively but also reduces the ecological toxicity of the resulting products, highlighting its potential for mitigating the environmental risks of TC contamination.

4. Conclusions

In this study, a highly efficient and stable $Cu_2S@Co_3S_4$ core-shell heterostructure catalyst was successfully fabricated and applied to activate H_2O_2 for the degradation of TC. The composite demonstrated superior catalytic performance compared to its individual components, achieving rapid and nearly complete TC removal under optimized conditions. The key findings and implications of this work are summarized as follows: (i) the $Cu_2S@Co_3S_4/H_2O_2$ system operated effectively over a wide pH range (5–11) and maintained robust performance in the presence of common anions, highlighting its potential for practical applications; (ii) a comprehensive mechanistic study unveiled that

$^1O_2$ produced from the activation of H_2O_2 at the catalyst interface rather than via energy transfer from dissolved oxygen, was the primary reactive species; (iii) DFT calculations and electrochemical analysis confirmed that internal electron transfer from the Cu_2S core to the Co_3S_4 shell created an electron-rich surface, which significantly strengthened H_2O_2 adsorption, facilitated O–O bond elongation, and promoted efficient electron transfer from TC to the oxidant; (iv) the identification of degradation intermediates and subsequent toxicity evaluation confirmed that the catalytic process effectively reduced the toxicity of the reaction products, thereby mitigating the environmental risk. In conclusion, this work not only presents $Cu_2S@Co_3S_4$ as a promising, durable catalyst for antibiotic wastewater treatment via H_2O_2 activation but also provides a profound and detailed understanding of the non-radical $^1O_2$ dominated mechanism and the critical role of interfacial electron transfer in heterostructure catalysts. The insights gained could guide the rational design of advanced catalytic materials for environmental remediation.

Acknowledgments

This work was financially supported by National Natural Science Foundation of China (52270004).

References

[1] Z. Lin, Y. Chen, G. Li, T. Wei, H. Li, F. Huang, W. Wu, W. Zhang, L. Ren, Y. Liang, Z. Zhen, D. Zhang, Change of tetracycline speciation and its impacts on tetracycline removal efficiency in vermicomposting with epigeic and endogeic earthworms, Science of The Total Environment 881 (2023) 163410. https://doi.org/10.1016/j.scitotenv.2023.163410.

[2] C. Li, Y. Ji, Y. Shi, X. Xu, L. Bao, M. Cui, Z. Tian, Z. Zhao, A smart Zn-MOF-based ratiometric fluorescence sensor for accurate distinguish and optosmart sensing of different types of tetracyclines, Applied Surface Science 640 (2023) 158442. https://doi.org/10.1016/j.apsusc.2023.158442.

[3] B. Liu, H. Zhu, R. Feng, M. Wang, P. Hu, J. Pan, X. Niu, Facile molecular imprinting on magnetic nanozyme surface for highly selective colorimetric detection of tetracycline, Sensors and Actuators B: Chemical 370 (2022) 132451. https://doi.org/10.1016/j.snb.2022.132451.

[4] Y. Amangelsin, Y. Semenova, M. Dadar, M. Aljofan, G. Bjørklund, The Impact of Tetracycline Pollution on the Aquatic Environment and Removal Strategies, Antibiotics 12 (2023) 440. https://doi.org/10.3390/antibiotics12030440.

[5] D. Wang, F. Jia, H. Wang, F. Chen, Y. Fang, W. Dong, G. Zeng, X. Li, Q. Yang, X. Yuan, Simultaneously efficient adsorption and photocatalytic degradation of tetracycline by Fe-based MOFs, Journal of Colloid and Interface Science 519 (2018) 273–284. https://doi.org/10.1016/j.jcis.2018.02.067.

[6] M. Coha, G. Farinelli, A. Tiraferri, M. Minella, D. Vione, Advanced oxidation processes in the removal of organic substances from produced water: Potential, configurations, and research needs, Chemical Engineering Journal 414 (2021) 128668. https://doi.org/10.1016/j.cej.2021.128668.

[7] R. Dewil, D. Mantzavinos, I. Poulios, M.A. Rodrigo, New perspectives for Advanced Oxidation Processes, Journal of Environmental Management 195 (2017) 93–99. https://doi.org/10.1016/j.jenvman.2017.04.010.

[8] Y. Liu, Y. Zhao, J. Wang, Fenton/Fenton-like processes with in-situ production of hydrogen peroxide/hydroxyl radical for degradation of emerging contaminants: Advances and prospects, Journal of Hazardous Materials 404 (2021) 124191. https://doi.org/10.1016/j.jhazmat.2020.124191.

[9] Y. Qu, Z. Chen, Y. Duan, L. Liu, H2O2 assisted photocatalysis over Fe-MOF modified BiOBr for degradation of RhB, Journal of Chemical Technology & Biotechnology 97 (2022) 2881–2888. https://doi.org/10.1002/jctb.7199.

[10] J. Wu, J. Zou, J. Lin, S. Li, L. He, Z. Wu, Q. Li, C. Gong, J. Ma, Overlooked Role of Coexistent Hydrogen Peroxide in Activated Peracetic Acid by Cu(II) for Enhanced Oxidation of Organic Contaminants, Environ. Sci. Technol. 58 (2024) 15741–15754. https://doi.org/10.1021/acs.est.3c09753.

[11] L. Tian, Z.-J. Tang, L.-Y. Hao, T. Dai, J.-P. Zou, Z.-Q. Liu, Efficient Homolytic Cleavage of H2O2 on Hydroxyl-Enriched Spinel CuFe2O4 with Dual Lewis Acid Sites, Angewandte Chemie International Edition 63 (2024) e202401434. https://doi.org/10.1002/anie.202401434.

[12] C.-C. Lin, Y.-H. Zhong, Degradation of Orange G in water by nano-Cu0/H2O2 process with nano-Cu0 synthesized in a rotating packed bed with blade packings, Materials Chemistry and Physics 295 (2023) 127097. https://doi.org/10.1016/j.matchemphys.2022.127097.

[13] L. Zhang, J. Chen, Y. Zhang, Y. Xu, T. Zheng, X. Zhou, Highly efficient activation of peracetic acid by nano-CuO for carbamazepine degradation in wastewater: The significant role of H2O2 and evidence of acetylperoxy radical contribution, Water Research 216 (2022) 118322. https://doi.org/10.1016/j.watres.2022.118322.

[14] P. Gholami, L. Dinpazhoh, A. Khataee, A. Hassani, A. Bhatnagar, Facile hydrothermal synthesis of novel Fe-Cu layered double hydroxide/biochar nanocomposite with enhanced sonocatalytic activity

for degradation of cefazolin sodium, Journal of Hazardous Materials 381 (2020) 120742. https://doi.org/10.1016/j.jhazmat.2019.120742.
[15] J. Li, A.N. Pham, R. Dai, Z. Wang, T.D. Waite, Recent advances in Cu-Fenton systems for the treatment of industrial wastewaters: Role of Cu complexes and Cu composites, Journal of Hazardous Materials 392 (2020) 122261. https://doi.org/10.1016/j.jhazmat.2020.122261.
[16] Y. Zhao, X. Shi, S.J.H. Ong, Q. Yao, B. Chen, K. Hou, C. Liu, Z.J. Xu, L. Guan, Enhancing the Charge Transportation Ability of Yolk–Shell Structure for High-Rate Sodium and Potassium Storage, ACS Nano 14 (2020) 4463–4474. https://doi.org/10.1021/acsnano.9b10045.
[17] R. Purbia, S. Paria, Yolk/shell nanoparticles: classifications, synthesis, properties, and applications, Nanoscale 7 (2015) 19789–19873. https://doi.org/10.1039/C5NR04729C.
[18] W. He, J. Zhang, S. Dieckhöfer, S. Varhade, A.C. Brix, A. Lielpetere, S. Seisel, J.R.C. Junqueira, W. Schuhmann, Splicing the active phases of copper/cobalt-based catalysts achieves high-rate tandem electroreduction of nitrate to ammonia, Nat Commun 13 (2022) 1129. https://doi.org/10.1038/s41467-022-28728-4.
[19] J. Zhang, W. He, T. Quast, J.R.C. Junqueira, S. Saddeler, S. Schulz, W. Schuhmann, Single-entity Electrochemistry Unveils Dynamic Transformation during Tandem Catalysis of Cu2O and Co3O4 for Converting NO3− to NH3, Angewandte Chemie International Edition 62 (2023) e202214830. https://doi.org/10.1002/anie.202214830.
[20] J. Zhang, T. Wang, D. Pohl, B. Rellinghaus, R. Dong, S. Liu, X. Zhuang, X. Feng, Interface Engineering of MoS2/Ni3S2 Heterostructures for Highly Enhanced Electrochemical Overall-Water-Splitting Activity, Angewandte Chemie International Edition 55 (2016) 6702–6707. https://doi.org/10.1002/anie.201602237.
[21] G. Zhang, Y. Wang, M. Chen, J. Xu, L. Wang, ZIF-67-derived carbon@Co3S4/CoSO4/MnO polyhedron to activate peroxymonosulfate for degrading levofloxacin: Synergistic effect and mechanism, Chemical Engineering Journal 451 (2023) 138976. https://doi.org/10.1016/j.cej.2022.138976.
[22] Z. Wang, Z. Wang, W. Li, Y. Lan, C. Chen, Performance comparison and mechanism investigation of Co3O4-modified different crystallographic MnO2 (α, β, γ, and δ) as an activator of peroxymonosulfate (PMS) for sulfisoxazole degradation, Chemical Engineering Journal 427 (2022) 130888. https://doi.org/10.1016/j.cej.2021.130888.
[23] M. Xing, W. Xu, C. Dong, Y. Bai, J. Zeng, Y. Zhou, J. Zhang, Y. Yin, Metal Sulfides as Excellent Co-catalysts for H2O2 Decomposition in Advanced Oxidation Processes, Chem 4 (2018) 1359–1372. https://doi.org/10.1016/j.chempr.2018.03.002.
[24] Y. Huang, L. Nengzi, X. Zhang, J. Gou, Y. Gao, G. Zhu, Q. Cheng, X. Cheng, Catalytic degradation of ciprofloxacin by magnetic CuS/Fe2O3/Mn2O3 nanocomposite activated peroxymonosulfate: Influence factors, degradation pathways and reaction mechanism, Chemical Engineering Journal 388 (2020) 124274. https://doi.org/10.1016/j.cej.2020.124274.
[25] M. Xu, H. Niu, J. Huang, J. Song, C. Mao, S. Zhang, C. Zhu, C. Chen, Facile synthesis of graphene-like Co3S4 nanosheet/Ag2S nanocomposite with enhanced performance in visible-light photocatalysis, Applied Surface Science 351 (2015) 374–381. https://doi.org/10.1016/j.apsusc.2015.05.158.
[26] W. Huang, W. Luo, J. Liu, B.-E. Jia, C. Lee, J. Dong, L. Yang, B. Liu, Q. Yan, Cascade Electrocatalytic Nitrate Reduction Reaching 100% Nitrate-N to Ammonia-N Conversion over Cu_2O@CoO Yolk–Shell Nanocubes, ACS Nano 18 (2024) 20258–20267. https://doi.org/10.1021/acsnano.4c03995.
[27] Y. Zhang, X. Yang, Y. Wang, P. Zhang, D. Liu, Y. Li, Z. Jin, B.B. Mamba, A.T. Kuvarega, J. Gui,

Insight into l-cysteine-assisted growth of Cu2S nanoparticles on exfoliated MoS2 nanosheets for effective photoreduction removal of Cr(VI), Applied Surface Science 518 (2020) 146191. https://doi.org/10.1016/j.apsusc.2020.146191.
[28] L. He, D. Zhou, Y. Lin, R. Ge, X. Hou, X. Sun, C. Zheng, Ultrarapid in Situ Synthesis of Cu2S Nanosheet Arrays on Copper Foam with Room-Temperature-Active Iodine Plasma for Efficient and Cost-Effective Oxygen Evolution, ACS Catal. 8 (2018) 3859–3864. https://doi.org/10.1021/acscatal.8b00032.
[29] Q. Cheng, C. Yang, K. Tao, L. Han, Inlaying ZIF-derived Co3S4 hollow nanocages on intertwined polypyrrole tubes conductive networks for high-performance supercapacitors, Electrochimica Acta 341 (2020) 136042. https://doi.org/10.1016/j.electacta.2020.136042.
[30] C. Tao, T. Shen, L. Ma, X. Zhang, C. Wang, G. Huang, S. Xu, Strategic design of NiS2/Co3S4 heterojunction for enhanced electrocatalytic hydrogen evolution in acidic media, International Journal of Hydrogen Energy 54 (2024) 1130–1136. https://doi.org/10.1016/j.ijhydene.2023.11.336.
[31] X. Li, T. Gao, H. Ma, E. Liu, B. Zhao, T. Sun, Highly efficient p-p heterojunction Co3S4/NiS2 electrocatalyst for water splitting and electrochemical oxidation of organic molecules, Applied Surface Science 678 (2024) 161127. https://doi.org/10.1016/j.apsusc.2024.161127.
[32] H. Zhang, C. Zhou, H. Zeng, H. Wu, L. Yang, L. Deng, Z. Shi, ZIF-8 assisted synthesis of magnetic core–shell Fe3O4@CuS nanoparticles for efficient sulfadiazine degradation via H2O2 activation: Performance and mechanism, Journal of Colloid and Interface Science 594 (2021) 502–512. https://doi.org/10.1016/j.jcis.2021.03.057.
[33] X. Zhang, B. Ren, X. Li, B. Liu, S. Wang, P. Yu, Y. Xu, G. Jiang, High-efficiency removal of tetracycline by carbon-bridge-doped g-C3N4/Fe3O4 magnetic heterogeneous catalyst through photo-Fenton process, Journal of Hazardous Materials 418 (2021) 126333. https://doi.org/10.1016/j.jhazmat.2021.126333.
[34] X. Xie, Y. Hu, H. Cheng, Rapid degradation of *p*-arsanilic acid with simultaneous arsenic removal from aqueous solution using Fenton process, Water Research 89 (2016) 59–67. https://doi.org/10.1016/j.watres.2015.11.037.
[35] Y.-Y. Chen, Y.-L. Ma, J. Yang, L.-Q. Wang, J.-M. Lv, C.-J. Ren, Aqueous tetracycline degradation by H2O2 alone: Removal and transformation pathway, Chemical Engineering Journal 307 (2017) 15–23. https://doi.org/10.1016/j.cej.2016.08.046.
[36] Y. Sun, F. Liu, Y. Gao, J. Dou, Y. Jiang, A. Deng, L. Zhao, H. Liu, Flower-Shaped MnFe2O4@MoS2 Nanocomposite Activated H2O2 for Efficient Degradation of Tetracycline: Performance Evaluation, Mechanism and Degradation Pathway, Catalysts 14 (2024) 738. https://doi.org/10.3390/catal14100738.
[37] W.-D. Oh, Z. Dong, T.-T. Lim, Hierarchically-structured Co–CuBi2O4 and Cu–CuBi2O4 for sulfanilamide removal *via* peroxymonosulfate activation, Catalysis Today 280 (2017) 2–7. https://doi.org/10.1016/j.cattod.2016.04.043.
[38] J.J. López Peñalver, C.V. Gómez Pacheco, M. Sánchez Polo, J. Rivera Utrilla, Degradation of tetracyclines in different water matrices by advanced oxidation/reduction processes based on gamma radiation, Journal of Chemical Technology & Biotechnology 88 (2013) 1096–1108. https://doi.org/10.1002/jctb.3946.
[39] T. Zhang, H. Zhu, J.-P. Croué, Production of Sulfate Radical from Peroxymonosulfate Induced by a Magnetically Separable CuFe2O4 Spinel in Water: Efficiency, Stability, and Mechanism, Environ. Sci. Technol. 47 (2013) 2784–2791. https://doi.org/10.1021/es304721g.
[40] H. Zeng, L. Deng, H. Zhang, C. Zhou, Z. Shi, Development of oxygen vacancies enriched CoAl hydroxide@hydroxysulfide hollow flowers for peroxymonosulfate activation: A highly efficient

singlet oxygen-dominated oxidation process for sulfamethoxazole degradation, Journal of Hazardous Materials 400 (2020) 123297. https://doi.org/10.1016/j.jhazmat.2020.123297.
[41] T. Peng, H. Zhang, S. Xia, S. Zhou, Z. Shi, G. Li, L. Deng, MoS2 Nanosheets Anchored onto MIL-100(Fe)-Derived FeS2 as a Peroxymonosulfate Activator for Efficient Sulfamethoxazole Degradation: Insights into the Mechanism, ACS EST Water 3 (2023) 213–226. https://doi.org/10.1021/acsestwater.2c00501.
[42] D. Wang, L. Zhao, H. Ma, H. Zhang, L.-H. Guo, Quantitative Analysis of Reactive Oxygen Species Photogenerated on Metal Oxide Nanoparticles and Their Bacteria Toxicity: The Role of Superoxide Radicals, Environ. Sci. Technol. 51 (2017) 10137–10145. https://doi.org/10.1021/acs.est.7b00473.
[43] X. Liu, M. Li, Z. Xie, P. Li, C. Du, Y. Su, Oxygen vacancy-enriched kaolinite/WO3-x nanocomposites exhibiting enhanced photo-synergetic H2O2 activation for tetracycline degradation boosted by hydroxyl groups and exciton, Separation and Purification Technology 347 (2024) 127675. https://doi.org/10.1016/j.seppur.2024.127675.
[44] X. Zhang, B. Yang, H. Quan, H. Pei, S.-Q. Guo, Surface methyl/methylene regulates WO3 directional activation of molecular oxygen into singlet oxygen for the removal of organic pollutants in water, Separation and Purification Technology 346 (2024) 127559. https://doi.org/10.1016/j.seppur.2024.127559.
[45] T. Ma, M. Liu, T. Li, H. Ren, R. Zhou, Nitrogen-doped carbon nanotubes derived from carbonized polyaniline as a robust peroxydisulfate activator for the oxidation removal of organic pollutants: Singlet oxygen dominated mechanism and structure-activity relationship, Separation and Purification Technology 293 (2022) 121124. https://doi.org/10.1016/j.seppur.2022.121124.
[46] J. Chang, S. Xia, Z. Shi, H. Zeng, H. Zhang, L. Deng, In situ anchoring of bimetal (Cu, Fe) sulfides featured by sulfur vacancy and phosphorus doping within porous carbon nanocubes derived from Prussian blue analogs to activate peroxymonosulfate for the efficient degradation of organic pollutants, Chemical Engineering Journal 498 (2024) 155252. https://doi.org/10.1016/j.cej.2024.155252.
[47] X. Ge, J. Xu, T. Zhou, L. Tian, W. Wang, X. Xu, J. Chen, X. Wang, Electronic Structure Reconfiguration of Zn-N_x B_{4-x} Sites for Enhanced Fenton-Like Catalysis, Angew Chem Int Ed 64 (2025) e202515736. https://doi.org/10.1002/anie.202515736.
[48] H. Zhang, C. Zhou, H. Zeng, L. Deng, Z. Shi, Can Cu2ZnSnS4 nanoparticles be used as heterogeneous catalysts for sulfadiazine degradation?, Journal of Hazardous Materials 395 (2020) 122613. https://doi.org/10.1016/j.jhazmat.2020.122613.
[49] Y. Shi, Y. Hu, Y. Wang, X. Li, C. Xiao, J. Liu, Y. Chen, J. Cheng, X. Zhu, G. Wang, J. Xie, 3D N-doped graphene aerogel sponge-loaded CoS2 co-catalytic Fenton system for ciprofloxacin degradation, Journal of Cleaner Production 380 (2022) 135008. https://doi.org/10.1016/j.jclepro.2022.135008.
[50] Z. Li, C. Wang, L. Zhao, H. Liu, J. Yang, X. Zhai, P. Ju, Q. Jiang, J. Duan, B. Hou, Sulfate-reducing bacteria-regulated Cu2O-doped Cu2S nanocubes as Fenton-like catalysts for efficient dye degradation and disinfection, Journal of Environmental Chemical Engineering 13 (2025) 117346. https://doi.org/10.1016/j.jece.2025.117346.
[51] Z. Shi, C. He, H. Huang, X. Huang, T. Hu, Y. He, D. Yang, S. Xia, H. Zhang, L. Deng, A novel polydopamine-loaded copper sulfide (CuS@PDA) for activating H2O2 to eliminate tetracycline via 1O2 dominated oxidation pathway, Journal of Water Process Engineering 71 (2025) 107223. https://doi.org/10.1016/j.jwpe.2025.107223.
[52] A.U. Khan, M. Kasha, Singlet molecular oxygen in the Haber-Weiss reaction., Proceedings of the National Academy of Sciences 91 (1994) 12365–12367. https://doi.org/10.1073/pnas.91.26.12365.

[53] X. Luo, H. Hu, Z. Pan, F. Pei, H. Qian, K. Miao, S. Guo, W. Wang, G. Feng, Efficient and stable catalysis of hollow Cu9S5 nanospheres in the Fenton-like degradation of organic dyes, Journal of Hazardous Materials 396 (2020) 122735. https://doi.org/10.1016/j.jhazmat.2020.122735.
[54] T. Luo, H. Feng, L. Tang, Y. Lu, W. Tang, S. Chen, J. Yu, Q. Xie, X. Ouyang, Z. Chen, Efficient degradation of tetracycline by heterogeneous electro-Fenton process using Cu-doped Fe@Fe2O3: Mechanism and degradation pathway, Chemical Engineering Journal 382 (2020) 122970. https://doi.org/10.1016/j.cej.2019.122970.
[55] J. Zeng, W. Xie, Y. Guo, T. Zhao, H. Zhou, Q. Wang, H. Li, Z. Guo, B.B. Xu, H. Gu, Magnetic field facilitated electrocatalytic degradation of tetracycline in wastewater by magnetic porous carbonized phthalonitrile resin, Applied Catalysis B: Environmental 340 (2024) 123225. https://doi.org/10.1016/j.apcatb.2023.123225.
[56] S. Xin, S. Huo, C. Zhang, X. Ma, W. Liu, Y. Xin, M. Gao, Coupling nitrogen/oxygen self-doped biomass porous carbon cathode catalyst with CuFeO2/biochar particle catalyst for the heterogeneous visible-light driven photo-electro-Fenton degradation of tetracycline, Applied Catalysis B: Environmental 305 (2022) 121024. https://doi.org/10.1016/j.apcatb.2021.121024.
[57] X. Li, K. Cui, Z. Guo, T. Yang, Y. Cao, Y. Xiang, H. Chen, M. Xi, Heterogeneous Fenton-like degradation of tetracyclines using porous magnetic chitosan microspheres as an efficient catalyst compared with two preparation methods, Chemical Engineering Journal 379 (2020) 122324. https://doi.org/10.1016/j.cej.2019.122324.
[58] B. Huo, F. Meng, J. Yang, Y. Wang, J. Qi, W. Ma, Z. Wang, J. Wang, Z. Wang, High efficiently piezocatalysis degradation of tetracycline by few-layered MoS2/GDY: Mechanism and toxicity evaluation, Chemical Engineering Journal 436 (2022) 135173. https://doi.org/10.1016/j.cej.2022.135173.

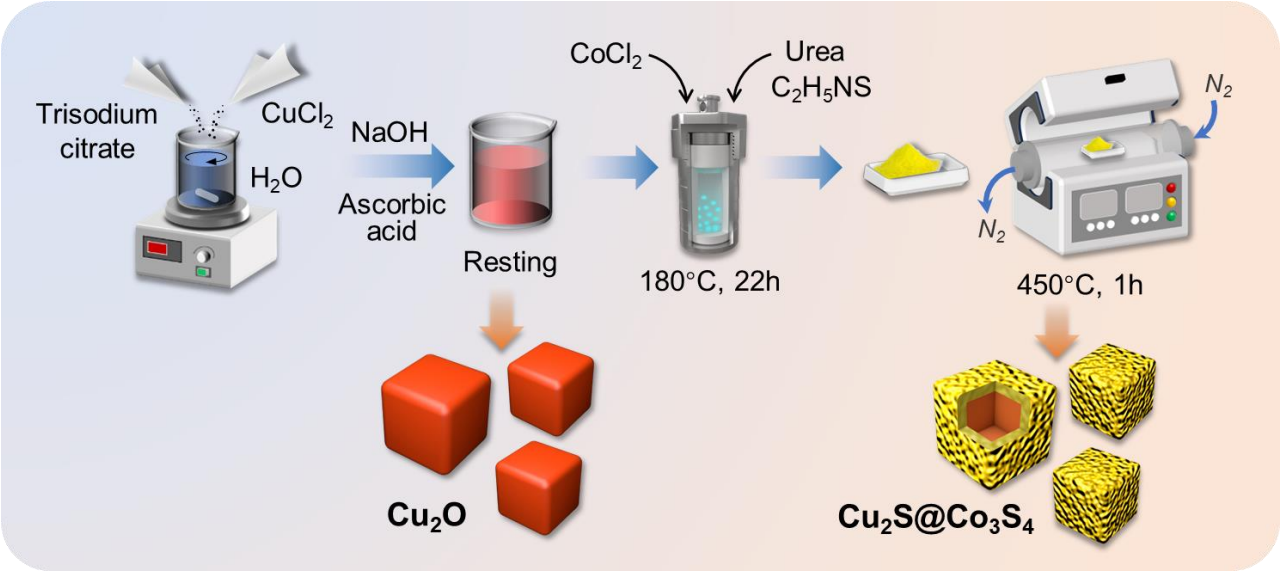

Scheme 1. The synthesis route of $Cu_2S@Co_3S_4$

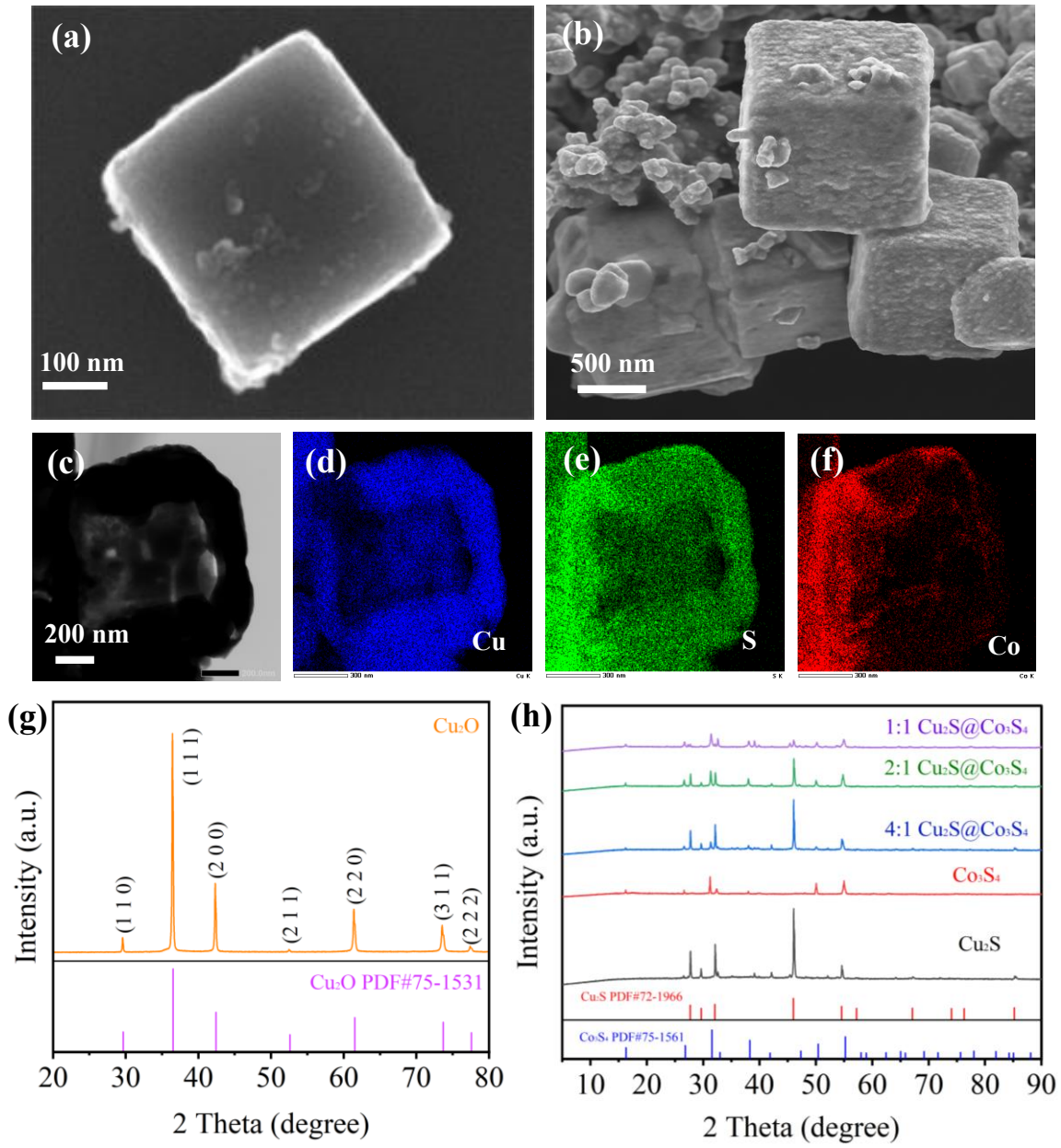

Figure 1. SEM images of (a) Cu_2O and (b) $Cu_2S@Co_3S_4$; (c) TEM image and (d-f) corresponding EDX mappings of $Cu_2S@Co_3S_4$; (g) XRD patterns of Cu_2O; and (h) XRD patterns of Cu_2S, Co_3S_4, and various $Cu_2S@Co_3S_4$ composites.

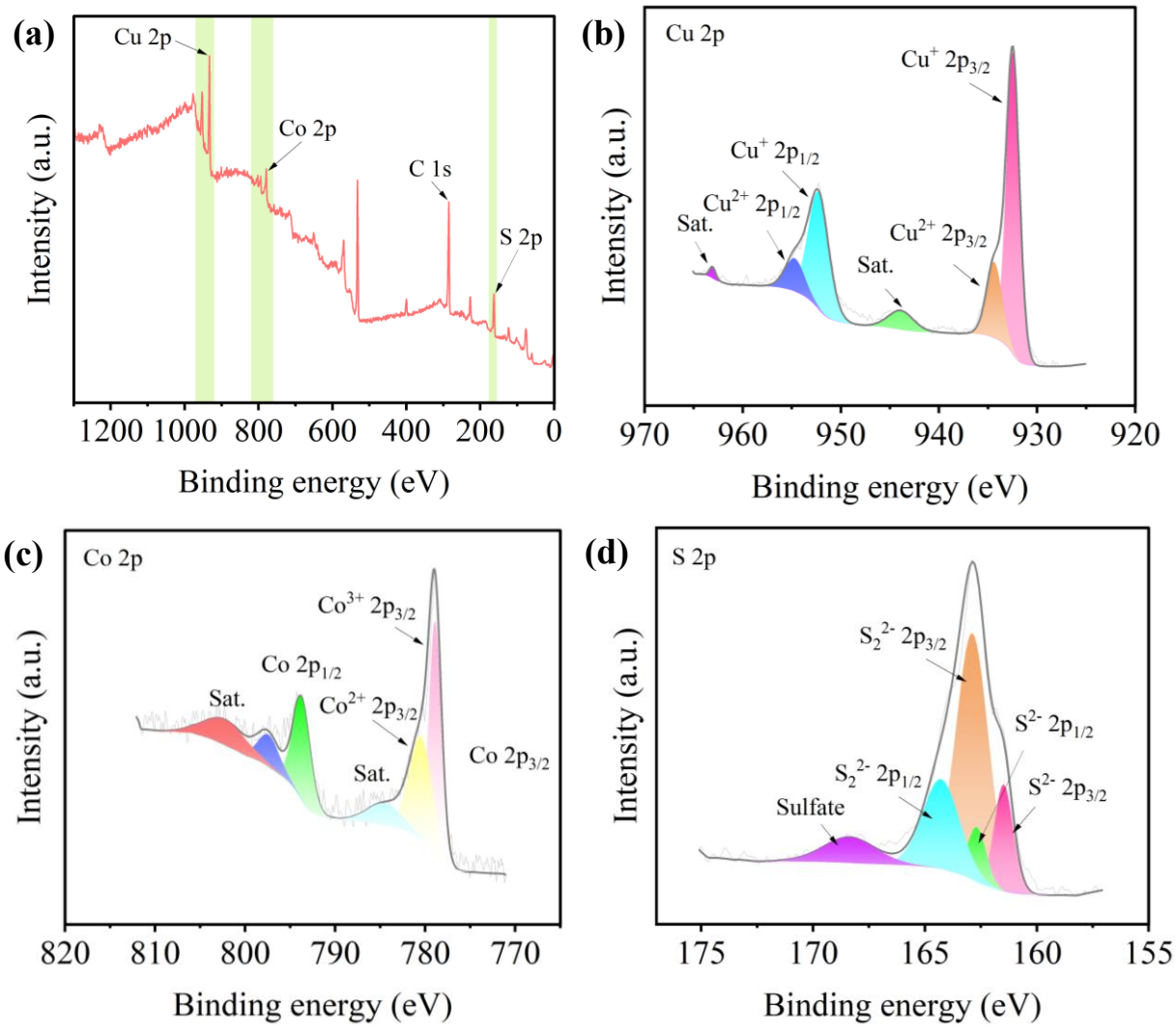

Figure 2. (a) XPS survey spectrum of $Cu_2S@Co_3S_4$; high-resolution XPS spectrum of (b) Cu 2p, (c) Co 2p, (d) S 2p.

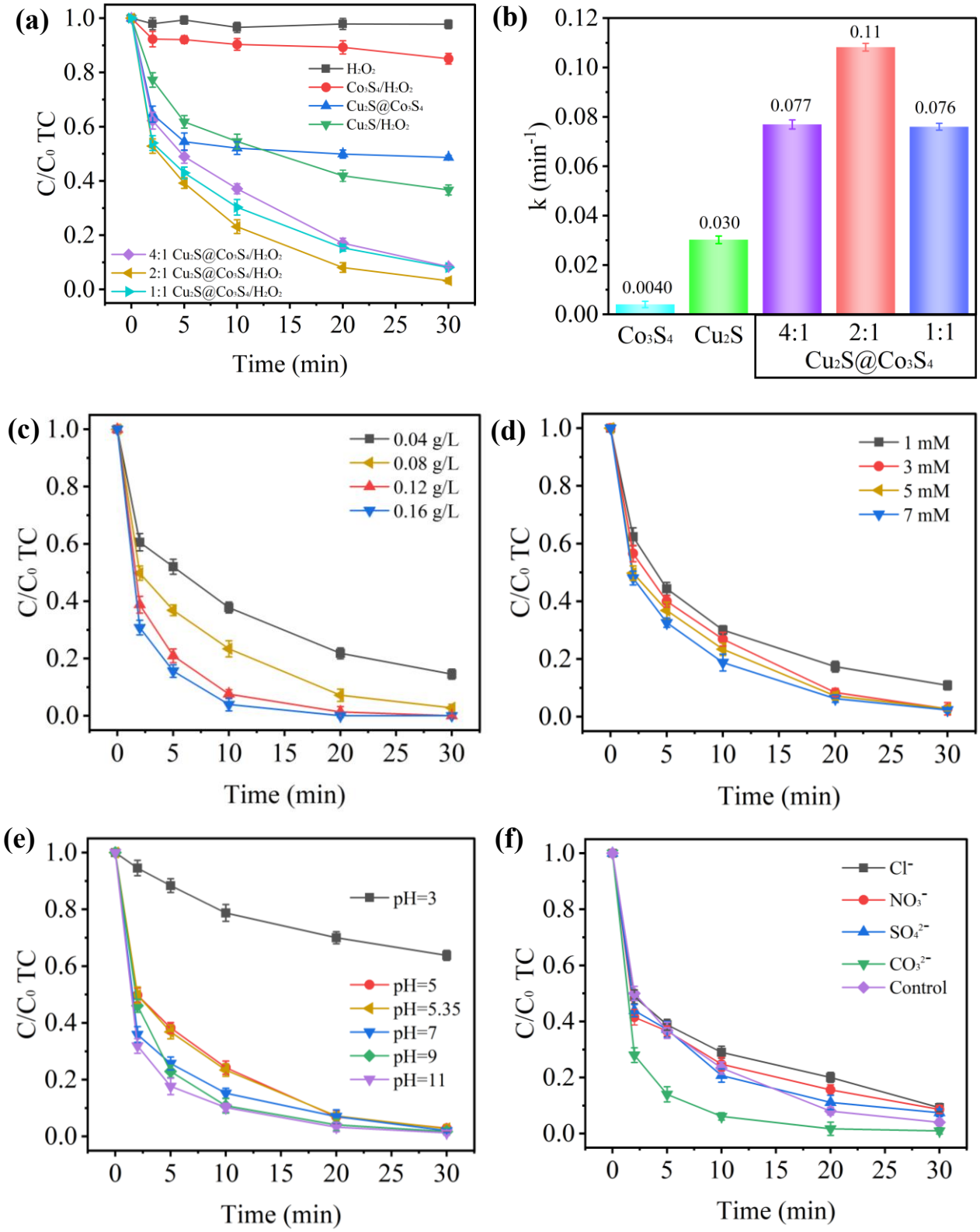

Figure 3. (a) Comparison of TC removal in different systems; (b) reaction rate constants achieved by Cu_2S, Co_3S_4, and various $Cu_2S@Co_3S_4$; effects of (c) catalyst dosage, (d) H_2O_2 concentration, (e) initial solution pH, and (f) coexisting ions on TC degradation by the $Cu_2S@Co_3S_4/H_2O_2$ system. ([TC] = 20 μM, [catalyst] = 0.08 g/ L, [H_2O_2] = 5 mM).

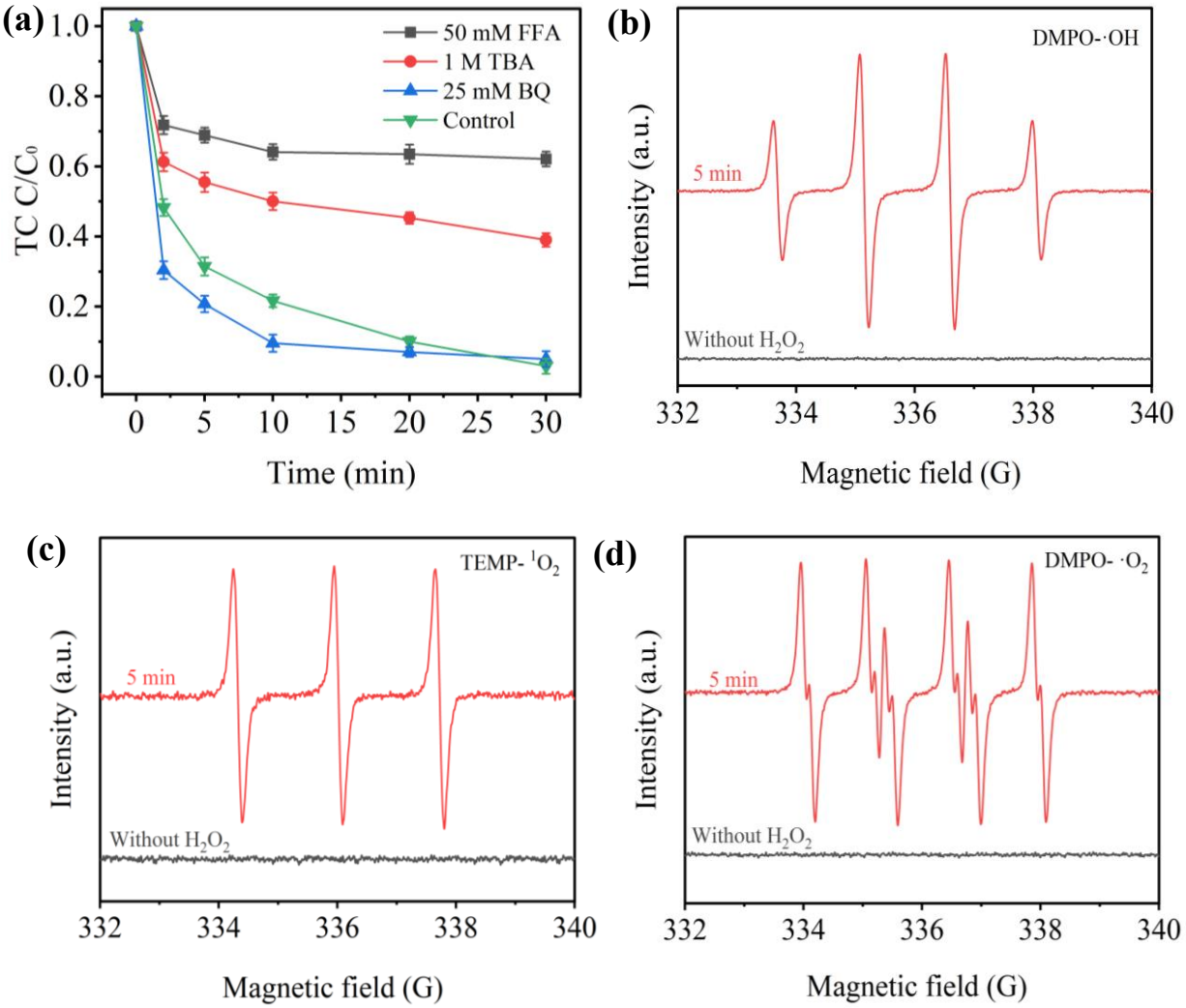

Figure 4. (a) Effect of different radical scavengers on the degradation of TC; EPR spectroscopy of (b) DMPO-•OH, (c) TEMP-$^1O_2$ and (d) DMPO-•O_2^-.

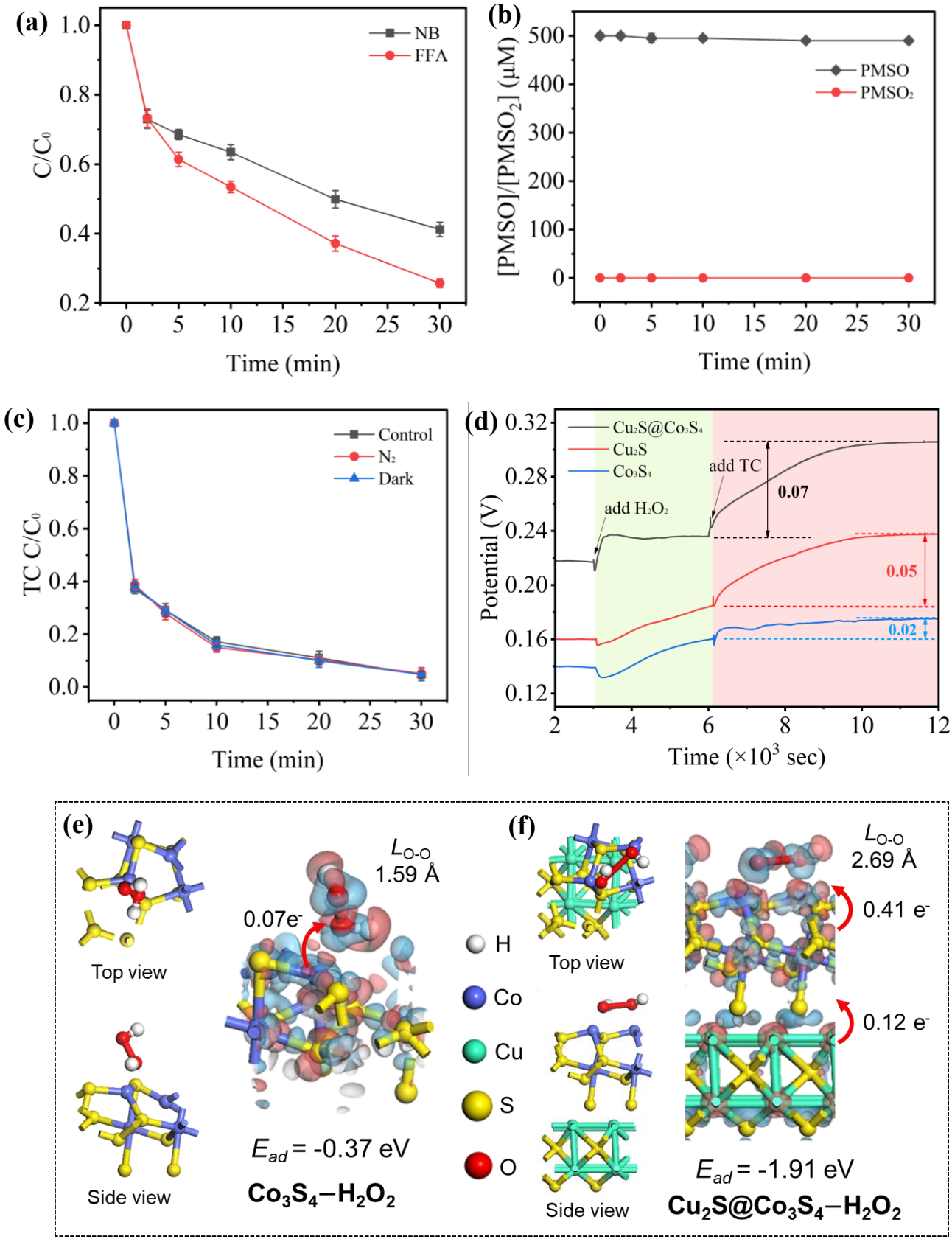

Figure 5. (a) Degradation effects on different radical trapping agents; (b) PMSO removal in $Cu_2S@Co_3S_4/H_2O_2$ system; (c) TC removal in $Cu_2S@Co_3S_4/H_2O_2$ system under different conditions. ([TC] = 20 μM, [catalyst] = 0.08 g/L, [H_2O_2] = 5 mM); (d) The open circuit potential of different systems; The composite structure and differential charge density of (e) Co_3S_4-H_2O_2 and (f) $Cu_2S@Co_3S_4$-H_2O_2 (The red and blue areas represent electron depletion and accumulation, respectively).

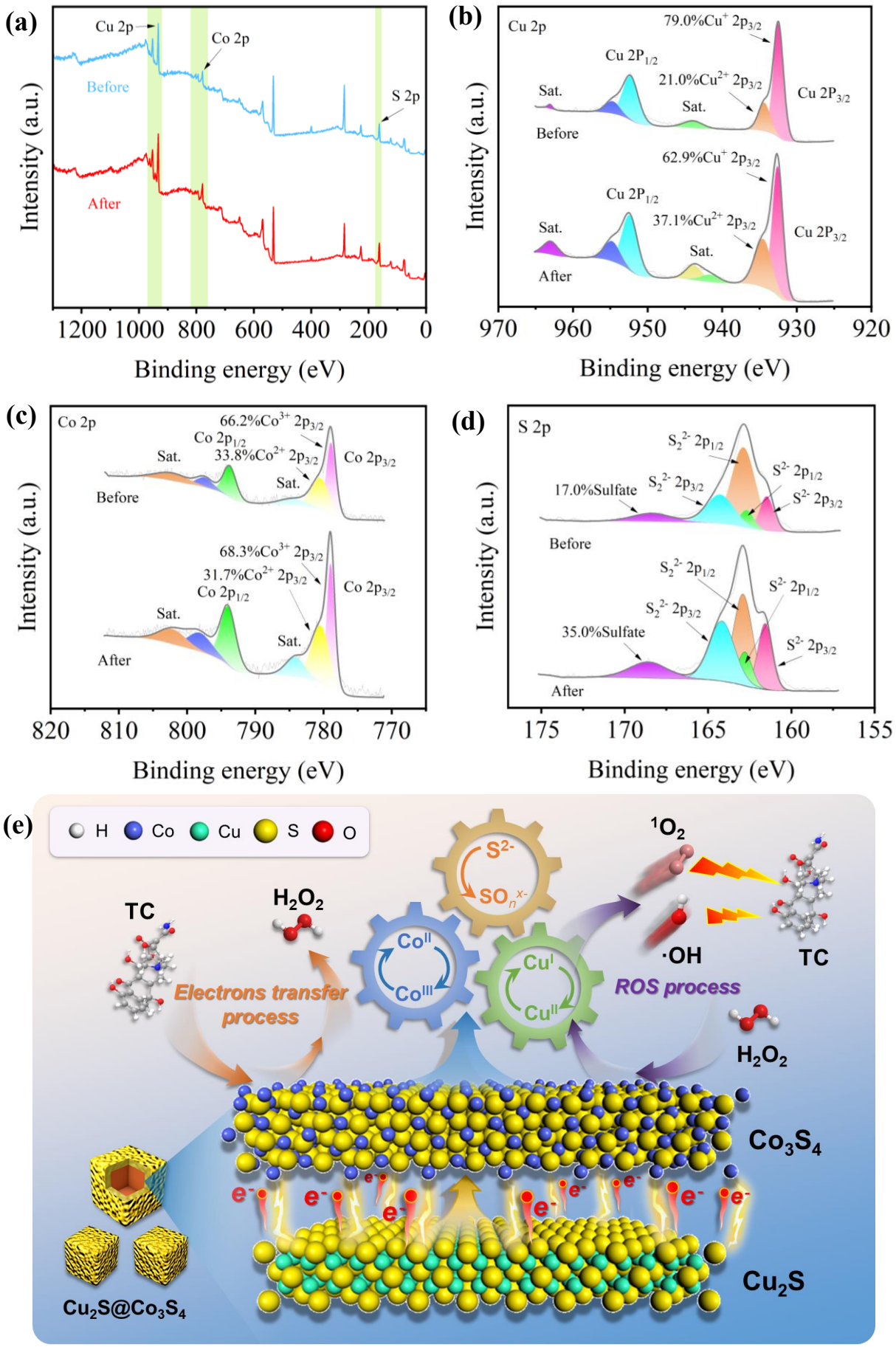

Figure 6. The XPS spectrum of $Cu_2S@Co_3S_4$ before and after reaction: (a) survey, (b) Cu 2p, (c) Co 2p, and (d) S 2p; (e) The proposed H_2O_2 activation mechanism in $Cu_2S@Co_3S_4/H_2O_2$ system.

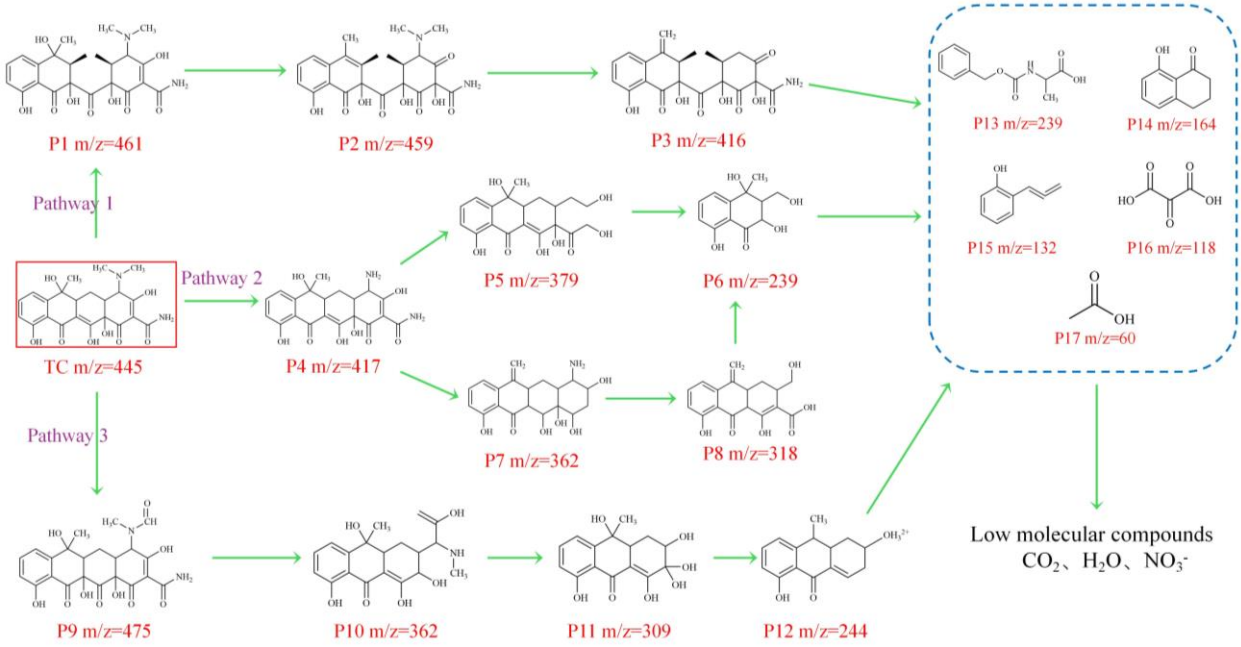

Figure 7. Possible degradation pathways of TC by the $Cu_2S@Co_3S_4/H_2O_2$ system.

Declaration of interests

☒The authors declare that they have no known competing financial interests or personal relationships that could have appeared to influence the work reported in this paper.

☐The authors declare the following financial interests/personal relationships which may be considered as potential competing interests: